Solid Freeform Fabrication 2024: Proceedings of the 35th Annual International Solid Freeform Fabrication Symposium – An Additive Manufacturing Conference
Reviewed Paper

Fused Deposition Modeling Using Orthogonally Configured Cartesian Printheads

J. Short*, B. Warner*, G. Shepherd*, D. L. Scruggs*, L. Southard*, H. Bai*, S. Farsiani*, R. Y. Azarfam†, H Noori*

* School of Mechanical and Aerospace Engineering, Oklahoma State University, Stillwater, OK, 74078
† Department of Chemistry, Oklahoma State University, Stillwater, OK, 74078

Abstract

A multi-axis extrusion-based 3D printer was developed with two printheads configured orthogonally to add counter-gravity printing capability to conventional gantry-based fused deposition modeling. Process settings, including layer height and print speed, could be customized for each printhead. Printheads could be controlled independently to manufacture products with customized spatial properties. The CAD models of products were sliced into at least two segments to prevent collision between printheads and designs. The primary printhead needed to start to create a part of the design as a substrate for the secondary printhead, which began its action when enough space was provided for its motion. Subsequently, the primary printhead could continue constructing on a part built by the secondary printhead.

The printheads were utilized to manufacture three-point bending samples comprising two longitudinal segments bonded in their thickness direction. The results showed that the segment configuration with respect to the loading direction can significantly influence flexural strength and crack initiation.

Nomenclature

b	sample's width
d	sample's thickness
L	support span
m	slope of the tangent to the initial linear portion of the load-punch displacement curve
P	maximum bending load
E_B	modulus of elasticity in bending
σ_f	flexural strength in the outer fiber at the midpoint

Introduction

Additive manufacturing of polymers and their composites accelerates the production of multifunctional designs [1-9]. The layer-by-layer construction of parts in 3D printing can provide opportunities to customize products' properties for specific service conditions [8-10]. For example, the layer's material, height, and orientation can be changed to customize printed parts' physical or mechanical properties [11-12]. Multi-axis fused deposition modeling offers a path forward to overcome the limitations for individualized processing of each layer using printers with only deposition direction along gravity force.

Multi-axis 3D printing can be classified into two main categories based on the printhead motions: cartesian and non-cartesian printing. Cartesian motion offers better precision in positioning and working safety [13-15]. On the other hand, non-cartesian-based robots are mostly preferred for multi-axis additive manufacturing due to their greater freedom in controlling the layers' orientation and their ability to print curved and conformal layers [16-22]. However, non-cartesian robots require more space for maneuvering, and incorporating multi-material printing capability increases hardware complexity. Nevertheless, compared to conventional single-axis gantry-based processing, multi-axis 3D printing is considered a processing technique that can improve product material and geometric properties [13-21]. Therefore, research and innovation are needed to address the challenges associated with multi-axis 3D printing, making it more user-friendly regarding hardware and software, cost-effective, and versatile in required printing accuracy, resolution, and materials selection for specific applications.

This paper introduces a novel polymer extrusion-based printer [22] with two printheads configured orthogonally, enabling layer deposition in gravity and counter-gravity directions. The conceptual design is shown in **Fig 1**. In addition to the design process, this work presents the three-point bending test results on manufactured samples involving segments with different deposition orientations through the samples' thickness.

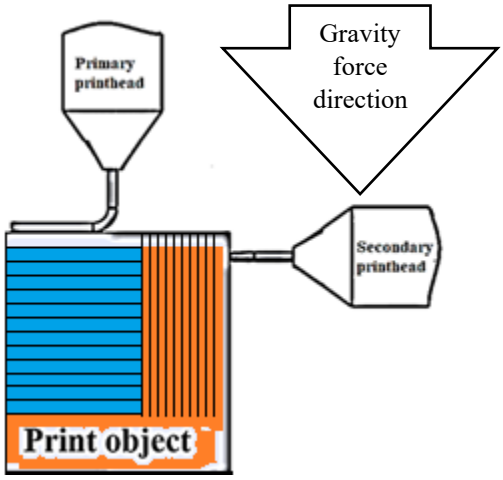

Fig. 1. Conceptual design of a two-axis 3D printer

Multi-axis 3D printer design

The multi-axis 3D printer (alpha prototype) was built on a four-column platform (Ender-5 Pro, Creality, China). As shown in **Fig. 2**, the printer structure was modified to install a second printhead orthogonal to the primary printhead. For this purpose, the frame of the printer was extended from one side to provide space for the secondary printhead. In addition, the added printhead was devised to have three degrees of freedom motion by adding a stepper motor for driving the printhead toward the print bed. The printheads in the current design could move independently. Therefore, CAD models were sliced by the operator to print each segment using a chosen printhead without collision between printheads. Since the print bed does not face the

secondary printhead, the primary printhead was utilized to manufacture a substrate for material deposition by the secondary printhead.

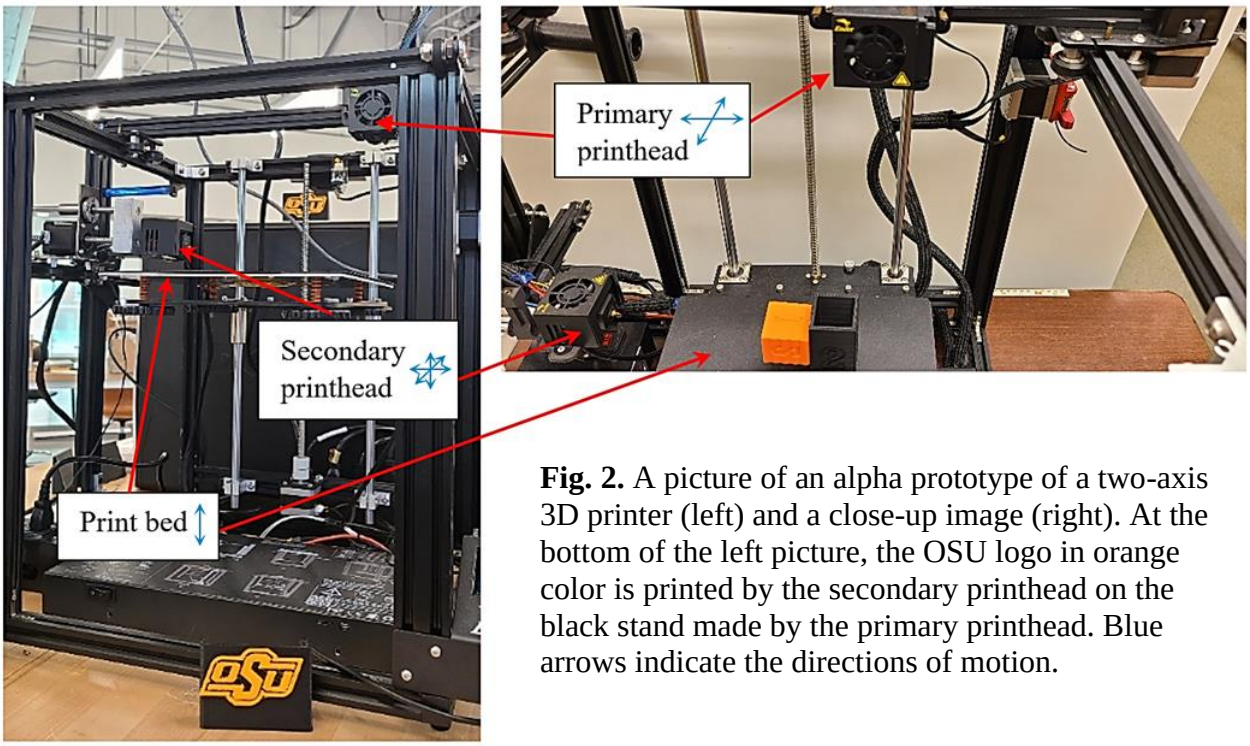

Fig. 2. A picture of an alpha prototype of a two-axis 3D printer (left) and a close-up image (right). At the bottom of the left picture, the OSU logo in orange color is printed by the secondary printhead on the black stand made by the primary printhead. Blue arrows indicate the directions of motion.

Three-point bending sample preparation

According to ASTM D790 [23], three-point bending experiments were conducted on PLA samples prepared by the multi-axis 3D printer. The samples shown in **Fig. 3** had two segments bonded in their thickness direction during 3D printing. The first segment (segment P) was printed with the primary printhead moving along X-Y directions. Segment S was manufactured consecutively by the secondary printhead moving along X-Z directions. The segments' length, width, and depth on their CAD models were 100, 15, and 2.5 mm, respectively. All print settings (nozzle temperature of 215 ºC, infill density of 10%, extrusion flow rate, layer height of 0.2 mm, and extrusion nozzle orifice diameter of 0.4 mm) were the same for all samples.

The ratio of support span to depth for bending samples was 16. The testing configurations differed in whether segment P (condition 1) or

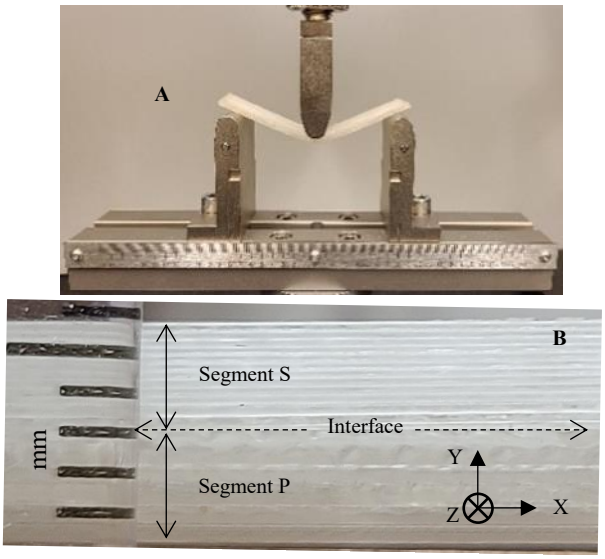

Fig. 3. (A) a sample on the bending fixture and (B) a close-up of the sample thickness composed of two segments (p and s) with different print directions are shown. Segments p and s were manufactured by the primary and secondary printheads, respectively.

segment S (condition 2) was in contact with the bending punch. Six samples for each configuration were tested at a 20 mm/min crosshead speed utilizing a universal testing machine (Instron 5982, US). The load-displacement curves were obtained, and maximum forces were recorded with an accuracy of ±0.5% of reading values.

Results and discussion

Three-point bend tests provided a quantitative assessment of the products' flexural strength (σ_f) and modulus of elasticity (E_B). Equations (1) and (2) [14] are used to calculate the maximum bending stress and modulus of elasticity. Since the samples are composed of two segments, the strength corresponded to the maximum load at the onset of interface debonding between segments or fracture of either segment.

$$\sigma_f = 3PL/(2bd^2) \quad (1)$$

$$E_B = \mathrm{m}L^3/(4bd^3) \quad (2)$$

where P is the maximum bending load, and b, d, and L are the samples' width, thickness, and support span, respectively. The parameter m is the slope of the tangent to the initial linear portion of the load-punch displacement curve.

Fig. 4 shows a typical load-displacement curve for each testing condition. Segment P (see Fig. 3) was in contact with the bending punch for test condition 1. For condition 2, segment S was in contact with the punch. The flexural strength and modulus of elasticity for both conditions are presented in **Table 1**.

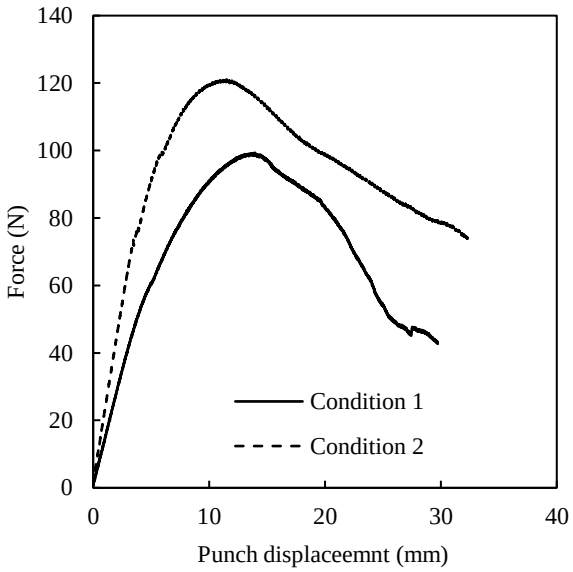

Fig. 4. Typical load-displacement curve for conditions 1 and 2 samples without interface fracture.

For samples without interface fracture, the average flexural strength and modulus for condition 2 were about 16% higher than those for condition 1 (37.7 vs. 32.4 MPa for strength and 1.21 vs. 1.40 GPa for modulus of elasticity). However, the flexural strength of samples with interface fracture was 21.1 MPa for both conditions.

Table 1. Bending properties of 3d printed samples

		Flexural strength (MPa)	Bending modulus of elasticity (GPa)
Condition 1	Average	32.4	1.21
	Standard deviation	2.47	0.23
Condition 2	Average	37.7	1.40
	Standard deviation	1.47	0.08

Higher flexural strength and modulus of elasticity for condition 2 can be attributed to the properties of segment P on the tension side of the bending sample. The friction between the punch and segment S for test condition 2 also contributed to the higher bending properties of the samples. The bending line was parallel and perpendicular to the built direction for segments P and S, respectively. It is, therefore, inferred that the performance of the printed structure by the multi-axis printer depends on the loading conditions and segments' orientation.

The fracture of the segments' interface can be due to the change in their built orientation from one segment to the other. Further studies are required to determine the effect of process parameters on the strength of the interface between the segments. Nonetheless, it is speculated that the multi-axis 3D printing process can customize the properties of the interface between segments. Therefore, the performance or fracture properties of 3D printed products can be customized to enhance the multifunctionality or repairability of the products.

Fractography

For condition 1, the fracture initiated at the outer fiber of segment S and propagated to segment P at the bending area, as shown in Figure 5(A). In this case, the crack propagated through the thickness, showing the effect of tensile stresses on the outer fibers of the specimen. For condition 2, the fracture was initiated either at the segments' interface or below the surface of segment S in contact with the punch. Although segment P was on the tension side of bending samples for condition 2, the fracture did not start at its outer fiber. Figure 5(B) shows the crack perpendicular to the bending line. Also, buckling was observed at the sides of the punch contact area, confirming the effect of compressive forces on the buckling of fibers of segment S. The buckling eventually led to crack initiation and propagation, which was different from the fracture of condition 1 samples. In addition to these fracture types, some samples experienced fracture at the interface between segments P and S, as shown in Figure 5(C and D).

These observations confirm that segment S, or the interface between segments, was preferred for crack initiation regardless of loading conditions. It is summarized that crack initiation or fracture path can be customized by changing the printing orientations of segments of the products manufactured by multi-axis 3D printers.

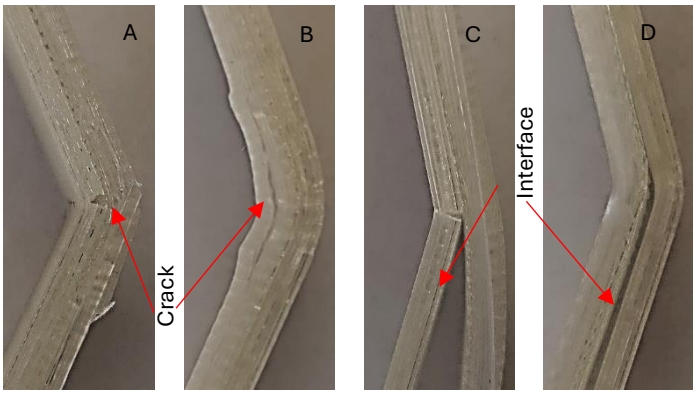

Fig. 5. Through-thickness fracture types: (A) condition 1 sample without interface debonding, (B) condition 2 sample without interface debonding, (C) interface fracture on condition 1, and (D) interface fracture on condition 2.

Conclusion

The concept of gantry-based multi-axis 3D printing, introduced in this paper, offers the potential for manufacturing multifunctional designs with customized spatial properties. Therefore, it opens new horizons in economical additive manufacturing complex designs with customized anisotropy applicable to medical, automotive, aerospace, and other industries.

References

[1] Ngo TD, Kashani A, Imbalzano G, Nguyen KTQ, Hui D (2018) Additive manufacturing (3D printing): A review of materials, methods, applications and challenges, Compos part B-Eng 143:172–196. DOI: 10.1016/j.compositesb.2018.02.012

[2] Ligon SC, Liska R, Stampfl J, Gurr M, Mülhaupt R (2017) Polymers for 3D printing and customized additive manufacturing, Chem. Rev. 117:10212−10290. DOI: 10.1021/acs.chemrev.7b00074

[3] Song Y, Li Y, Song W, Yee K, Lee K.-Y, Tagarielli VL (2017) Measurements of the mechanical response of unidirectional 3D-printed PLA, Mater. Des. 123:154–164. DOI: 10.1016/j.matdes.2017.03.051

[4] Chacón JM, Caminero MA, García-Plaza E, Núñez PJ (2017) Additive manufacturing of PLA structures using fused deposition modelling: Effect of process parameters on mechanical properties and their optimal selection, Mater. Des. 124:143–157. DOI: 10.1016/j.matdes.2017.03.065

[5] Aliheidari N, Christ J, Tripuraneni R, Nadimpalli S, Ameli A (2018) Interlayer adhesion and fracture resistance of polymers printed through melt extrusion additive manufacturing process, Mater. Des. 156:351–361. DOI: 10.1016/j.matdes.2018.07.001

[6] Popescu D, Zapciu A, Amza C, Baciu F, Marinescu R (2018) FDM process parameters influence over the mechanical properties of polymer specimens: A review, Polym. Test. 69:157–166. DOI: 10.1016/j.polymertesting.2018.05.020

[7] Mohamed OA, Masood SH, Bhowmik JL (2017) Experimental investigation of time-dependent mechanical properties of PC-ABS prototypes processed by FDM additive manufacturing process, Mater. Lett. 193:58–62. DOI: 10.1016/j.matlet.2017.01.104

[8] Jung JW, Lee J-S, Cho D-W (2016) Computer-aided multiple-head 3D printing system for printing of heterogeneous organ/tissue constructs, Sci. Rep. 6:21685. DOI: 10.1038/srep21685

[9] Butt J, Onimowo DA, Gohrabian M, Sharma T, Shirvani H (2018) A desktop 3D printer with dual extruders to produce customised electronic circuitry, Front. Mech. Eng. 13(4):528–534. DOI: 10.1007/s11465-018-0502-1

[10] Haque, N, Azarfam, MY, Noori, H (2021) Microwave-assisted fracture toughness improvement in additively manufactured polylactic acid–copper composite, J. Mat. Sci. 56(19):11298-11308. DOI:10.1007/s10853-021-06019-5

[11] Noori, H. (2019) Interlayer fracture energy of 3D-printed PLA material, Int. J. Adv. Manuf. Tech., 101(5-8):1959-1965. DOI:10.1007/s00170-018-3031-5

[12] Noori, H., and Lytle CC, (2020) Effect of counter-gravity 3D printing on PLA interlayer fracture energy. DOI: 10.1007/978-3-030-36296-6_23.

[13] Morita T., Watanabe S., Sasaki S. (2023) Multiaxis printing method for bent tubular structured gels in support bath for achieving high dimension and shape accuracy, Precis. Eng., 79: 109-118. DOI: 10.1016/j.precisioneng.2022.09.004

[14] Gupta E., Bonner C., Lazarus N., Mirotznik M.S., Nicholson K.J. (2023) Multiaxis Manufacture of Conformal Metasurface Antennas, IEEE Antennas Wirel. Propag. Lett., 22(11):2629-2633. DOI: 10.1109/LAWP.2023.3282556

[15] Wang T., Tong Q., Zhang Q., Yang H. (2023) Research of tangential additive manufacturing based on multiaxis and contour blades, Int. J. Adv. Manuf. Tech., 128(1-2): 789-799. DOI: 10.1007/s00170-023-11972-3

[16] Dai F., Zhang S., Li R., Zhang H. (2022) Multiaxis wire and arc additive manufacturing for overhangs based on conical substrates, Rapid Prototyping J., 28(1):126-142. DOI: 10.1108/RPJ-12-2020-0300

[17] Krčma M., Paloušek D., (2022) Comparison of the effects of multiaxis printing strategies on large-scale 3D printed surface quality, accuracy, and strength, Int. J. Adv. Manuf. Tech., 119 (11-12):7109-7120. DOI: 10.1007/s00170-022-08685-4

[18] Rauch M., Hascoet J.-Y., Querard V. (2021) A multiaxis tool path generation approach for thin wall structures made with WAAM, J. Manuf. Mater. Process., 5(4):128. DOI: 10.3390/jmmp5040128

[19] Krčma M., Paloušek D., Škaroupka D., Braumann J., Koutný D. (2023) Method of multiaxis three-dimensional printing with intralayer height variation for stairstep effect compensation, 3D Print. Addit. Manuf., 10(6): 1178-1189. DOI: 10.1089/3dp.2022.0097

[20] Gardner J.A., Nethercott-Garabet T., Kaill N., Campbell R.I., Bingham G.A., Engstrøm D.S., Balc NO (2020) Aligning material extrusion direction with mechanical stress via 5-axis tool paths, Proceedings of the 29th Annual International Solid Freeform Fabrication Symposium - SFF 2018, 2005-2019.

[21] Kubalak, J.R., Wicks, A.L. and Williams, C.B. (2019), Exploring multi-axis material extrusion additive manufacturing for improving mechanical properties of printed parts, Rapid Prototyping J., 25(2):356-362. DOI: 10.1108/RPJ-02-2018-0035

[22] Noori H. Multi-axis 3D printer. Publication of WO2023244642A1. 2023 December 21. Available from: https://patents.google.com/patent/WO2023244642A1/en#patentCitations Other: WO2023244642A1

[23] ASTM Designation D790- Standard test methods for flexural properties of unreinforced and reinforced plastics and electrical insulating materials, ASTM, Philadelphia, PA. DOI: 10.1520/D0790-17.